ACS APPLIED MATERIALS & INTERFACES

Research Article

www.acsami.org

Insights into the Performance Limits of the $Li_7P_3S_{11}$ Superionic Conductor: A Combined First-Principles and Experimental Study

Iek-Heng Chu, Han Nguyen, Sunny Hy, Yuh-Chieh Lin, Zhenbin Wang, Zihan Xu, Zhi Deng, Ying Shirley Meng,* and Shyue Ping Ong*

Department of NanoEngineering, University of California, San Diego, 9500 Gilman Drive, Mail Code 0448, La Jolla, California 92093, United States

Supporting Information

ABSTRACT: The $Li_7P_3S_{11}$ glass-ceramic is a promising superionic conductor electrolyte (SCE) with an extremely high Li^+ conductivity that exceeds that of even traditional organic electrolytes. In this work, we present a combined computational and experimental investigation of the material performance limitations in terms of its phase and electrochemical stability, and Li^+ conductivity. We find that $Li_7P_3S_{11}$ is metastable at 0 K but becomes stable at above 630 K (~360 °C) when vibrational entropy contributions are accounted for, in agreement with differential scanning calorimetry measurements. Both scanning electron microscopy and the calculated Wulff shape show that $Li_7P_3S_{11}$ tends to form relatively isotropic crystals. In terms of electrochemical stability, first-principles calculations predict that, unlike the $LiCoO_2$ cathode, the olivine $LiFePO_4$ and spinel $LiMn_2O_4$ cathodes are likely to form stable passivation interfaces with the $Li_7P_3S_{11}$ SCE. This finding underscores the importance of considering multicomponent integration in developing an all-solid-state architecture. To probe the fundamental limit of its bulk Li^+ conductivity, a comparison of conventional cold-press sintered versus spark-plasma sintering (SPS) $Li_7P_3S_{11}$ was done in conjunction with *ab initio* molecular dynamics (AIMD) simulations. Though the measured diffusion activation barriers are in excellent agreement, the AIMD-predicted room-temperature Li^+ conductivity of 57 mS cm^{-1} is much higher than the experimental values. The optimized SPS sample exhibits a room-temperature Li^+ conductivity of 11.6 mS cm^{-1}, significantly higher than that of the cold-pressed sample (1.3 mS cm^{-1}) due to the reduction of grain boundary resistance by densification. We conclude that grain boundary conductivity is limiting the overall Li^+ conductivity in $Li_7P_3S_{11}$, and further optimization of overall conductivities should be possible. Finally, we show that Li^+ motions in this material are highly collective, and the flexing of the P_2S_7 ditetrahedra facilitates fast Li^+ diffusion.

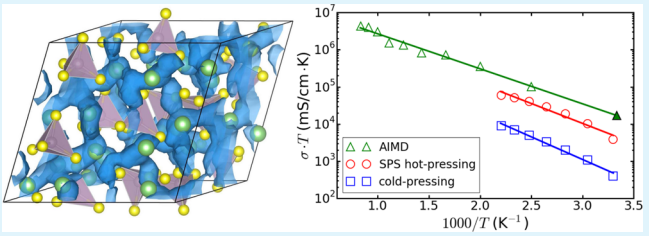

KEYWORDS: *superionic conductor electrolyte, $Li_7P_3S_{11}$, ionic conductivity, electrolyte−electrode interface, spark-plasma sintering, ab initio molecular dynamics*

INTRODUCTION

Rechargeable all-solid-state lithium-ion batteries utilizing a fast lithium superionic conductor electrolyte (SCE)[1−5] have the potential to revolutionize energy storage by providing an inherently safer, less flammable alternative to traditional organic electrolyte-based batteries.[6−8] The discovery of the $Li_{10}GeP_2S_{12}$[3,9] and $Li_7P_3S_{11}$[4,5,10−13] glass-ceramic conductors have provided further optimism that SCEs with Li^+ conductivities rivaling that of organic solvents exist. In particular, a room-temperature ionic conductivity of 17 mS cm^{-1} has been achieved in the $Li_7P_3S_{11}$ glass-ceramic,[5] which is the highest ionic conductivity observed for a SCE thus far.

$Li_7P_3S_{11}$ crystallizes in a triclinic structure with space group of $P\bar{1}$ (Int. No. 2),[4] as illustrated in Figure 1. All Li sites are fully occupied, with phosphorus and sulfur atoms forming individual PS_4 tetrahedra or S-sharing P_2S_7 ditetrahedra. The primitive cell consists of two formula units with seven symmetrically distinct lithium sites.

$Li_7P_3S_{11}$ was first reported by Mizuno et al. as the metastable crystal precipitated from $70Li_2S{\cdot}30P_2S_5$, with a room-temperature ionic conductivity of 3.2 mS cm^{-1}.[10,11] Its crystal structure was subsequently characterized by Yamane and co-workers.[4] Further optimization of heat treatment and high-pressure conditions during the synthesis process by Seino and co-workers produced a material with a room-temperature ionic conductivity of 17 mS cm^{-1},[5] which they attributed to the reduction of grain boundary impedance and thus reducing overall cell resistance. Such ionic conductivity even exceeds that of the $Li_{10}GeP_2S_{12}$ family of electrolytes.[3,9,14−16] On the computational front, Onodera et al.[17,18] applied the reverse Monte Carlo (RMC) approach and found that the lithium ionic conduction pathway, formed by LiS_4 tetrahedra linked with vacant S_4 tetrahedra, can be remarkably long. They hypothesized that the large number of vacant S_4 tetrahedra surrounding the Li ions is the origin of the high ionic conductivity in this compound. Lepley and Holzwarth[19] also

Received: January 21, 2016
Accepted: March 7, 2016

DOI: 10.1021/acsami.6b00833
ACS Appl. Mater. Interfaces XXXX, XXX, XXX−XXX

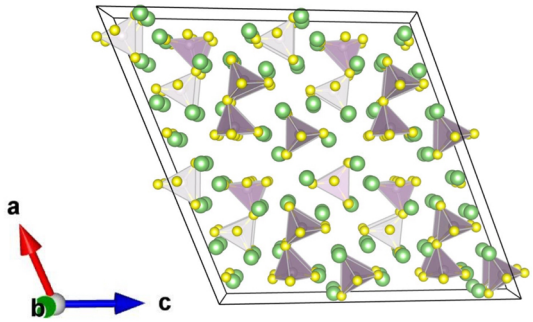

Figure 1. Crystal structure of a 2 × 2 × 2 supercell of $Li_7P_3S_{11}$. The tetrahedra are PS_4, and Li and S atoms are labeled with green and yellow spheres, respectively.

carried out a density functional theory (DFT) study of $Li_7P_3S_{11}$ and concluded that it is metastable and that the migration barrier along the *b* crystallographic direction (around 150 meV) is lower than along the other two crystallographic directions.

In this work, we build on the existing body of knowledge on the highly promising $Li_7P_3S_{11}$ SCE and present a comprehensive computational and experimental investigation of the performance limits of this material in terms of its phase and electrochemical stability, and Li^+ conductivity. We show that $Li_7P_3S_{11}$ is entropically stabilized at temperatures above 630 K (~360 °C) and tends to form relatively isotropic crystals. We demonstrate that the synthesis approach has a significant effect on the overall conductivity but only a small effect on measured activation energies. While a significant increase in conductivity from 1.3 to 11.6 mS cm^{-1} was experimentally observed by a densification process, *ab initio* molecular dynamics simulations predict $Li_7P_3S_{11}$ to have aan even higher bulk room-temperature Li^+ conductivity of 57 mS cm^{-1}. We also discuss the role of ionic motion correlation and the framework structure in facilitating fast Li^+ diffusion.

COMPUTATIONAL METHODS AND DETAILS

All calculations were performed using the Vienna *ab initio* simulation package (VASP)[20] under the projector augmented wave approach.[21] A structural optimization of the experimental $Li_7P_3S_{11}$ structure was first carried out,[4] and the fully relaxed structure was used in the subsequent calculations. Unless otherwise indicated, all calculations were spin-polarized and utilized the Perdew–Burke–Ernzerhof (PBE) generalized-gradient approximation (GGA)[22] exchange-correlation functional, a kinetic energy cutoff of 520 eV, and a Monkhorst–Pack *k*-mesh[23] with density of 1000/(number of atoms in the unit cell). All analyses were performed using the Python Materials Genomics (pymatgen) library.[24]

Phase Stability. The Li–P–S phase diagram at 0 K was constructed by determining the convex hull[25] of the composition-energy coordinates of all $Li_xP_yS_z$ compounds. Precomputed data were obtained from the Materials Project (MP)[26] using the Materials API.[27] The energy difference between the $Li_7P_3S_{11}$ phase and the predicted phase equilibria, also known as the energy above the hull (E_{hull}), was evaluated.[25] The E_{hull} is always non-negative and becomes zero for stable compounds. The higher the E_{hull}, the less stable the compound is predicted to be. A constant energy correction of −0.66 eV per S atom, which is similar to the scheme proposed by Wang et al.[28] for the O_2 molecule, was applied to the elemental sulfur energy.[29]

Dynamical Stability. Phonon calculations were carried out with a 1 × 2 × 1 supercell of $Li_7P_3S_{11}$ using the Phonopy package.[30] Real-space force constants associated with the atoms in the supercell were first computed within the framework of density-functional perturbation theory (DFPT),[31] and the phonon spectrum was then obtained by solving the dynamical matrices of various high-symmetry wave vectors. Thermodynamic quantities such as Gibbs free energy and vibrational entropy were computed from the phonon spectrum (see the Supporting Information (SI) for details).

Electrochemical Stability. The electrochemical stability of the SCEs in contact with the electrodes was estimated using two thermodynamic approximations.

(1) The first approximation is based on the previous work by Ong et al.,[14] which assumes that Li is the main mobile species. Under such conditions, the SCE–electrode interface can be modeled as an open system with respect to Li. The relevant thermodynamic potential is then the grand potential, given as $\phi = E - \mu_{Li} N_{Li}$, where E, N_{Li}, and μ_{Li} are respectively the internal energy, the number of Li atoms in the open system, and the Li chemical potential. The SCE–anode interface is modeled as the SCE material at high $\mu_{Li} \approx \mu^0_{Li}$, and the SCE–cathode interface is modeled as the SCE material at low $\mu_{Li} \approx \mu^0_{Li} - 5$ eV. Here, μ^0_{Li} is the energy of metallic Li.

(2) The second approximation assumes full thermodynamic equilibrium between the SCE and electrode in varying ratios. In essence, the pseudobinary phase diagram between SCE and electrode is constructed to identify the stable phase equilibria. This methodology is similar in spirit with previous work by Miara et al.,[32] but, in our approach, there is no assumption of the alkali ion being the dominant mobile species and composition conservation is enforced for all species. We believe this approach is more reflective of the conditions during actual synthesis and assembly conditions.

Electronic Structure. The band gap of an SCE serves as a measure of its electronic conductivity, as well as an upper limit for its intrinsic electrochemical window.[33] We performed electronic structure calculations using the Heyd–Scuseria–Ernzerhof (HSE) hybrid functional,[34,35] which has been shown to be significantly more accurate at predicting band gaps compared to semilocal functionals.[36] Due to the higher computational load compared to PBE calculations, a reduced Monkhorst–Pack *k*-mesh 2 × 4 × 2 was adopted instead.

Surface Energies and Wulff Shape. The surface energies for all surfaces with maximum index of 2 of $Li_7P_3S_{11}$ were calculated using the following expression:

$$\gamma = \frac{E_s - E_b}{2A} \quad (1)$$

where E_s and E_b represent the total energy of the slab and bulk, respectively, and A is the surface area. The normal width of the slab was set to at least 10 Å, and a 10 Å vacuum layer was added in the calculation to minimize interactions between periodic images. We further impose the conditions that PS_4^{3-} and $P_2S_7^{4-}$ polyhedra with highly covalent P–S bonds must remain intact, and only nonpolar surfaces were calculated. The equilibrium morphology of the $Li_7P_3S_{11}$ crystal was determined from the surface energies via the Wulff construction.[37]

Diffusivity and Ionic Conductivity. The diffusivity and conductivity of $Li_7P_3S_{11}$ were calculated using non-spin-polarized *ab initio* molecular dynamics (AIMD) simulations. A smaller plane-wave energy cutoff was selected as 280 eV. A 1 × 2 × 1 supercell along with a minimal Γ-centered 1 × 1 × 1 *k*-mesh were adopted. The time step was set to 2 fs. The simulation setup is similar to previous work by the authors.[38] The diffusivity was then obtained by performing a linear fitting of the mean square displacement (MSD) with time. Diffusivities were obtained at temperatures between 400 K and 1200 K in 100 K increments. Then an Arrhenius plot of ionic conductivity ($\sigma(T)$), as computed using the resulting diffusivities ($D(T)$) via the Nernst–Einstein relation,

$$\sigma(T)T = \frac{\rho z^2 F^2}{R} D(T) \quad (2)$$

was generated and used to determine the activation energy (E_a). Here, ρ is the molar density of diffusing ions in the unit cell. F, R, and z are the Faraday constant, the gas constant, and the charge of lithium ions that equals +1, respectively. A linear extrapolation was made to obtain the room-temperature conductivity. To analyze the correlations between ion motions, we calculated the self and distinct parts of the

DOI: 10.1021/acsami.6b00833
ACS Appl. Mater. Interfaces XXXX, XXX, XXX–XXX

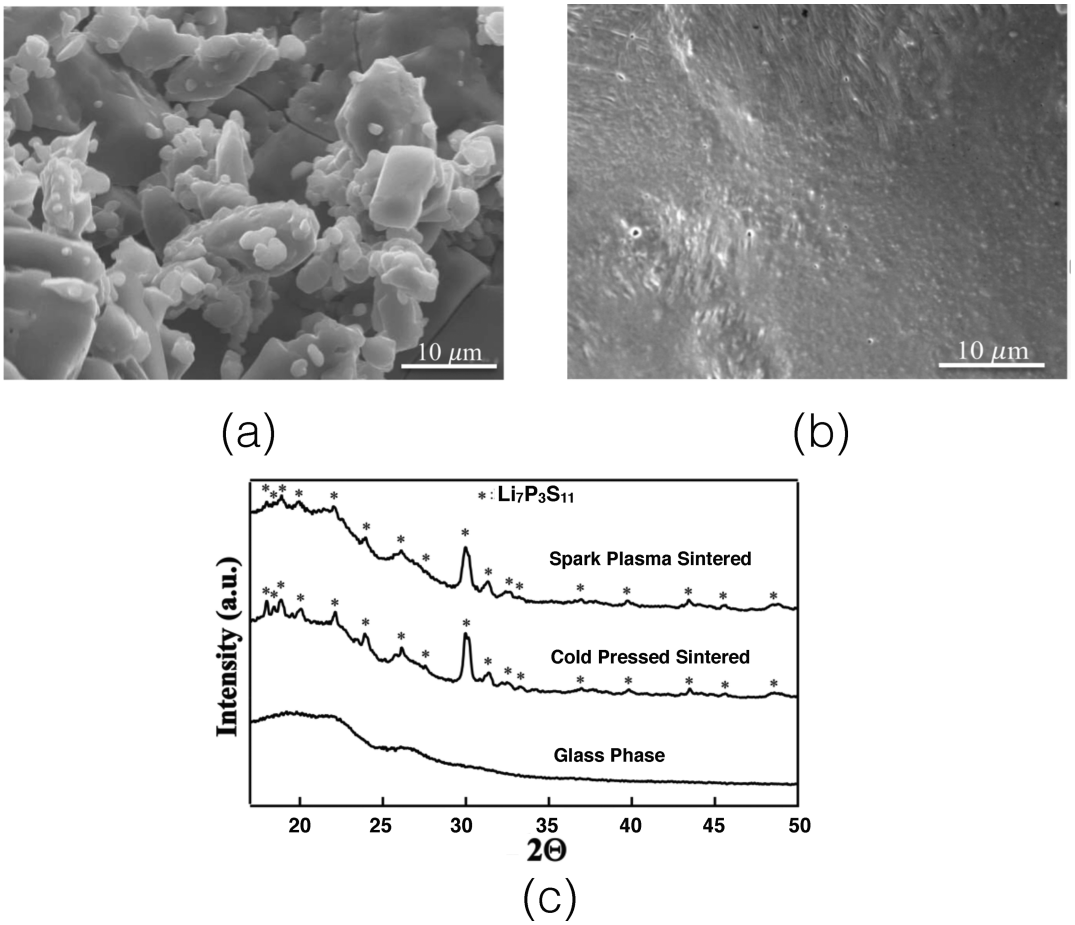

Figure 2. SEM images of (a) cold-pressed and (b) SPS $Li_7P_3S_{11}$ glass-ceramics. (c) XRD patterns of $70Li_2S{\cdot}30P_2S_5$ glass sintered by conventional methods and SPS.

van Hove correlation function from the AIMD trajectories, as detailed in our recent work.[29] A detailed description of these methods is also provided in the SI. We also investigated the Li^+ diffusion pathways by calculating the probability density distribution, which is defined on a uniform 3D grid in the unit cell (Ω) and obtained by ensemble averaging over the Li^+ ionic trajectories of AIMD in conjunction with $\int_\Omega P(\mathbf{r})\, d\mathbf{r} = 1$.[29] The van Hove and also the diffusion pathway analyses were performed using the pymatgen-diffusion add-on to pymatgen.[39]

EXPERIMENTAL METHODS

Synthesis. $70Li_2S{\cdot}30P_2S_5$ glass was synthesized from reagent-grade chemicals, P_2S_5 (Sigma-Aldrich, 99%) and Li_2S (Sigma-Aldrich 99.98%). Stoichiometric amounts of these chemicals were mixed and sealed in a quartz ampoule and heated at 973 K (700 °C) for 4 h. The molten sample was then quenched to room temperature in ice water. Subsequently, the resulting glass was ground for 30 min with an agate mortar and pestle into a glass powder. For the cold-pressed sample, the glass powder was sealed in a quartz ampoule, heated at 573 K (300 °C) for 2 h, and then quenched to room temperature in ice water. For the spark-plasma-sintered (SPS) samples, the glass powder was loaded into 10 mm tungsten−carbide dies, lined with a graphite sheet and pressed lightly. The loaded die was placed into the SPS chamber and pressed to a preload pressure of 10 MPa. The heating and pressure profiles were as follows: 573 K (300 °C) at a rate of 100 K/min and 300 MPa at a rate of 100 MPa/min. The temperature and applied pressure dwell times were 5 min. The experiment was conducted under flowing argon gas.

Characterization. Cross-sectional images of cold-pressed and SPS samples were collected with Phillips XL30 scanning electron microscopy (SEM). A thin film of iridium was coated onto the electronically insulating materials for use in the SEM. Iridium was sputtered onto the electrolyte materials by using an Emitech sputter coater for 7 s, with a current of 8 μA. SEM images were collected with an applied voltage of 20 kV.

X-ray diffraction (XRD) data of glass and glass-ceramic were collected by Rigaku diffractometer, using Cu Kα radiation. The scan range was 10°−70°.

The glass-transition temperature (T_g) and the glass-ceramic crystallization temperature (T_c) were determined by differential scanning calorimetry (DSC; PerkinElmer Pyris Diamond). The temperature range was from room temperature to 673 K (400 °C) with a scan rate of 10 K/min. The glass material was hermetically sealed in aluminum pans, and measurements were conducted under argon purging.

Electrochemical Measurements. Ionic conductivities were measured using electrochemical impedance spectroscopy (EIS) with an impedance analyzer (Solartron 1260) in the frequency range of 1 MHz to 1 Hz with an applied AC voltage of 25 mV. The diameters of the cold-pressed pellets and the SPS pellets were 13 mm and 10 mm, respectively. Cold-pressed pellets were pressed using 5 t while SPS pellets were used as is. Carbon paste was attached to both sides of the pellets as electrodes, and stainless steel plates were used as current collectors.

High-temperature conductivity measurements on the cold-pressed and SPS pellets were collected by heating the pellets in an electric furnace from room temperature to 453 K in 25 K increments. The solid electrolyte cell was heated in the electric furnace at a rate of 10 K/min to avoid temperature overshoot. Conductivity measurements were made after the cell had dwelled at the desired temperature for 1 h. The activation energy (E_a) for Li-ion diffusion was obtained from

DOI: 10.1021/acsami.6b00833
ACS Appl. Mater. Interfaces XXXX, XXX, XXX−XXX

Table 1. Cell Parameters of $Li_7P_3S_{11}$ Reported in Previous Experimental Studies and This Work

a (Å)	b (Å)	c (Å)	α (deg)	β (deg)	γ (deg)	
12.501	6.032	12.530	102.845	113.202	74.467	ref4
12.483	6.031	12.499	102.906	113.304	74.495	ref17
12.586	6.061	12.607	102.937	113.166	74.756	SPS hot-pressing, this work
12.493	6.030	12.532	102.834	113.265	74.524	cold-pressing, this work
12.84	6.20	12.64	103.72	113.78	74.09	DFT-PBE, this work

the Arrhenius plot. All measurements and heating were conducted in an Ar atmosphere.

RESULTS

Crystal Structure and Characterization. Panels a and b of Figure 2 show the SEM images of $Li_7P_3S_{11}$ crystals obtained from the cold-pressed and SPS heat treatment processes, respectively. It is clear that the morphology of the cold-pressed pellet is highly granular and contains a network of open pores, which is in contrast to the morphology of the SPS made pellets that exhibit much smoother surfaces. This is in line with the previous experimental report.[5]

Figure 2c shows the XRD patterns for the glass powder, cold-pressed glass-ceramic, and SPS glass-ceramic. The bottom curve shows the pattern of the melt-quenched precursors. No crystalline peaks from the two starting materials are present, and an amorphous glass phase is achieved when the molten material is quenched in ice water. Subsequent heat treatment of the glass phase material to form the glass-ceramic shows the $Li_7P_3S_{11}$ phase formed in both cold-pressed-sintered and SPS samples. The peaks observed in the cold-pressed-sintered and SPS glass-ceramics are identified as the glass-ceramic $Li_7P_3S_{11}$, which are in excellent agreement with the reported crystal structure by Yamane et al.[4] A comparison of the cell parameters estimated via XRD refinement and from DFT calculations in this work with previous experimental values in the literature is given in Table 1. Our experimental lattice parameters are in good agreement with previous works,[4,17] while the PBE calculated lattice parameters are consistently overestimated by 1−3% compared to the experimental values, which can be attributed to the well-known tendency for GGA functionals to underbind.

Phase Stability. Figure 3 shows the calculated Li−P−S phase diagrams at 0 K. Regardless of whether a sulfur correction is applied, $Li_7P_3S_{11}$ is predicted to be metastable at 0 K. However, the predicted phase equilibria at the $Li_7P_3S_{11}$ composition depends on whether the sulfur correction is applied.

In the absence of a sulfur correction, the predicted phase equilibrium is

$$Li_7P_3S_{11} \rightarrow Li_3PS_4 + Li_4P_2S_6 + S \quad (3)$$

and $Li_7P_3S_{11}$ is predicted to have an E_{hull} of 27 meV/atom. This result is consistent with the previous work by Lepley et al.[19] Here, Li_3PS_4 refers to the γ phase ($Pmn2_1$; ICSD id, 180318), which is energetically more stable at low temperatures, and $Li_4P_2S_6$ has space group $P6_3/mcm$ (ICSD id, 33506). For $Li_4P_2S_6$, we performed an enumeration of the disordered ICSD structure and used the lowest energy ordering in computing the phase diagrams.

With the incorporation of the sulfur correction, however, the local phase triangles change and the predicted phase equilibria is given by the following reaction:

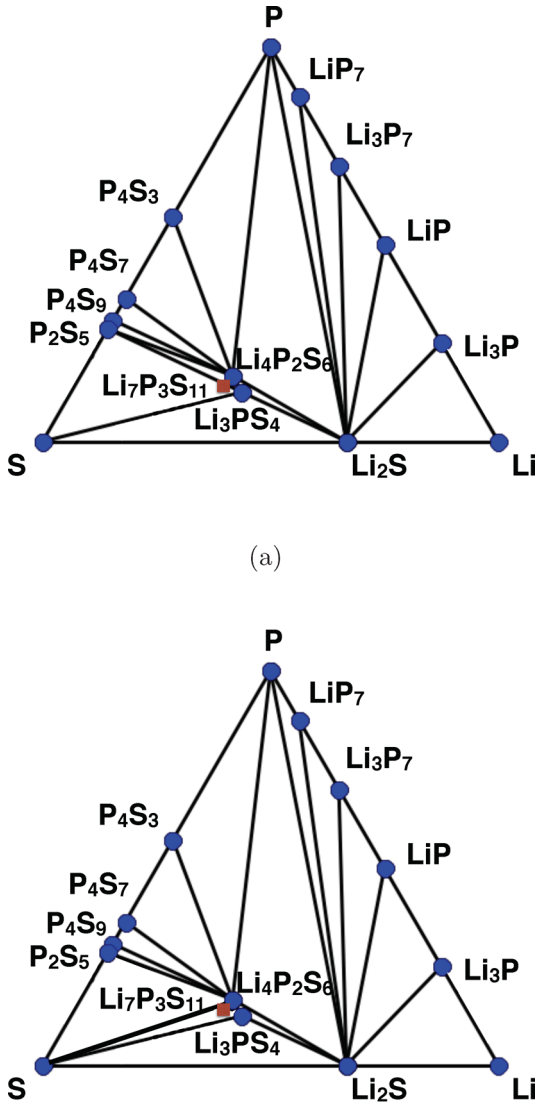

Figure 3. Li−P−S phase diagram at zero temperature (a) with and (b) without sulfur energy correction. Stable compounds are indicated as blue dots, whereas the metastable $Li_7P_3S_{11}$ is labeled with a brown square.

$$3Li_7P_3S_{11} \rightarrow 7Li_3PS_4 + P_2S_5 \quad (4)$$

and $Li_7P_3S_{11}$ is predicted to have an E_{hull} of 21 meV/atom. Here, P_2S_5 refers to the lowest energy phase in the MP database, which has space group $P\bar{1}$ and ICSD id 409061.

To estimate the transition temperature at which $Li_7P_3S_{11}$ becomes thermodynamically stable, the vibrational contributions to the entropy were estimated by computing the phonon

DOI: 10.1021/acsami.6b00833
ACS Appl. Mater. Interfaces XXXX, XXX, XXX−XXX

spectra for $Li_7P_3S_{11}$, Li_3PS_4 and P_2S_5 (see Figure S1 in the SI). Figure 4a plots the Gibbs free energy change of the reverse of

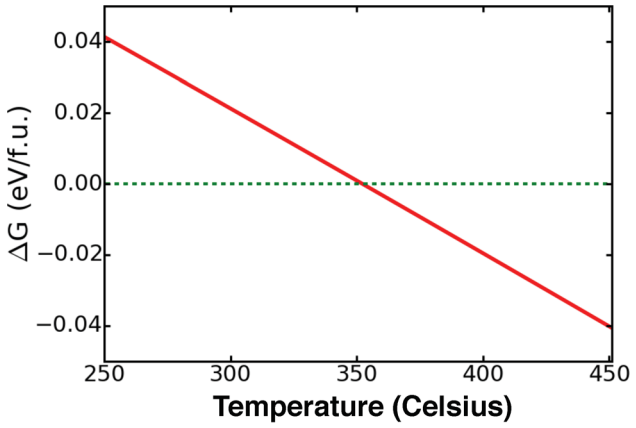

(a)

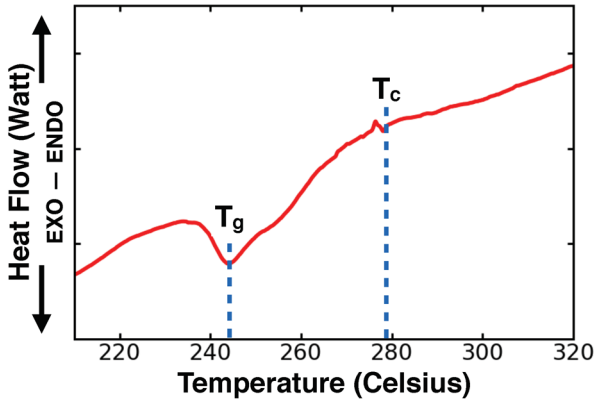

(b)

Figure 4. (a) Gibbs free energy change from P_2S_5 and Li_3PS_4 to $Li_7P_3S_{11}$ (ΔG; eV per formula unit of $Li_7P_3S_{11}$) as a function of temperature (red solid). The green dashed line indicates zero ΔG. (b) Experimental DSC curve of $70Li_2S{\cdot}30P_2S_5$ glass. Blue dashed lines denote the glass-transition temperature (T_g) and crystallization temperature (T_c).

reaction (4), $\Delta G(T)$, with respect to temperature. It can be observed that the free energy change becomes negative at temperatures greater than 630 K (~360 °C), which corresponds to the transition temperature.

Figure 4b shows the DSC measurement of $Li_7P_3S_{11}$. A shift in the baseline at around 518 K (245 °C) indicates that the material underwent a glass transition at T_g. Upon further heating, the crystallization temperature (T_c) was observed around 553 K (280 °C) and was followed by another shift in the baseline measurement, indicative of a change in heat capacity. The crystalline phase that was formed slightly above T_c was identified with XRD and found to be the metastable $Li_7P_3S_{11}$ crystal. Overall, the computed transition temperature of 630 K (~360 °C) is in excellent agreement with the measured crystallization temperature of $Li_7P_3S_{11}$ of 553 K (280 °C), as well as that reported previously.[5]

Electrochemical Stability. The lithium grand potential phase diagrams at $\mu_{Li} = \mu^0_{Li}$ and $\mu^0_{Li} - 5$ eV, corresponding to the $Li_7P_3S_{11}$ interface with a Li metal anode and a 5 V charged cathode environment, respectively, are given in Figure S2 in the SI. We find that, in the limit of fast Li mobility, the phase equilibria at the Li anode comprise Li_3P and Li_2S, whereas P_2S_5 and S are found at the 5 V charged cathode.

We also investigated the possible compounds formed at the $Li_7P_3S_{11}$/electrode interfaces with varying compositional ratios. Figure 5 shows the pseudobinary phase diagrams and phase equilibria (in Table 2) that depend on the ratio between $Li_7P_3S_{11}$ and (a) a CoO_2 charged cathode, (b) a $LiCoO_2$ discharged cathode, or (c) a Li metal anode. At the $Li_7P_3S_{11}$/Li interface, we find that the predicted phase equilibria comprise γ-Li_3PS_4, $Li_4P_2S_6$, Li_2S, and Li_xP_y compounds, which are all reasonable ionic conductors and poor electronic conductors that may form the basis of a good passivating layer. We also note that the phase equilibria at G in Figure 5c is in line with that predicted by the lithium grand potential approach. This is expected because Li is the only mobile species at the Li anode, and G corresponds to $Li_7P_3S_{11}$ reacting with an excess of Li.

However, at the $Li_7P_3S_{11}$/cathode interface, the predicted equilibrium phases depend strongly on the particular stoichiometry and cathode chemistry. The presence of products that involve Co, P, or S is consistent with previous experimental findings, where the mutual diffusions of Co, P, and S were observed at the interface formed between a Li_2S–P_2S_5 glass and $LiCoO_2$.[40] The formation of cobalt sulfides (*e.g.*, Co_3S_4) near the $Li_7P_3S_{11}$/$LiCoO_2$ interface also agrees well with a recent experimental report.[41] In general, we find that the $Li_7P_3S_{11}$/$LiCoO_2$ interface phase equilibria contain poor electronic

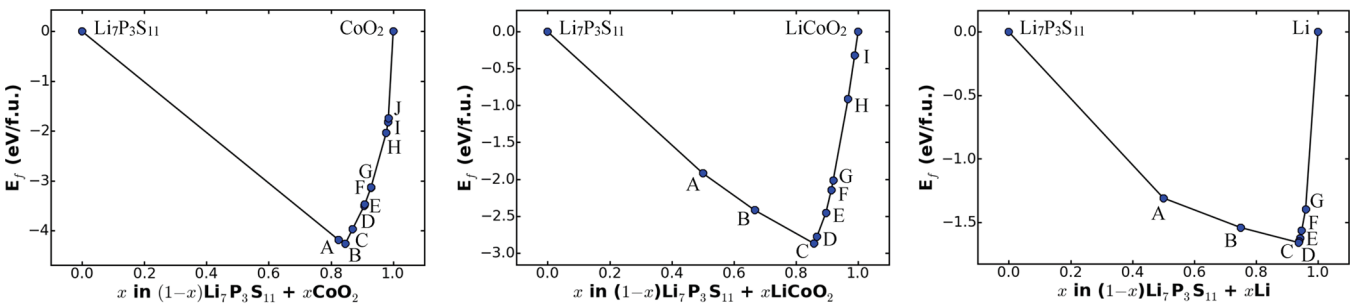

(a) (b) (c)

Figure 5. Pseudobinary phase diagrams between (a) $Li_7P_3S_{11}$ and CoO_2 charged cathode, (b) $Li_7P_3S_{11}$ and $LiCoO_2$ discharged cathode, and (c) $Li_7P_3S_{11}$ and metallic Li anode. Labeled reactions in the panels are given in Table 2.

DOI: 10.1021/acsami.6b00833
ACS Appl. Mater. Interfaces XXXX, XXX, XXX−XXX

Table 2. Phase Equilibria of $Li_7P_3S_{11}$ at (a) CoO_2 Charged Cathode, (b) $LiCoO_2$ Discharged Cathode, and (c) Metallic Li Anode As Labeled in Figure 5[a]

label	x	phase equilibria
(a) CoO_2		
A	0.8235	0.8235 $\underline{CoS_2}$ + 0.0588 P_2S_5 + 0.4118 Li_3PO_4
B	0.8462	0.8462 $\underline{CoS_2}$ + 0.1538 $Li_4P_2O_7$ + 0.1538 Li_3PO_4
C	0.8696	0.1739 $LiCoPO_4$ + 0.6957 $\underline{CoS_2}$ + 0.0435 Li_2SO_4 + 0.2174 Li_3PO_4
D	0.9067	0.2667 $LiCoPO_4$ + 0.2133 $\underline{Co_3S_4}$ + 0.1733 Li_2SO_4 + 0.0133 Li_3PO_4
E	0.9091	0.2727 $LiCoPO_4$ + 0.0076 $\underline{Co_9S_8}$ + 0.1894 $\underline{Co_3S_4}$ + 0.1818 Li_2SO_4
F	0.9283	0.1055 $Co_3(PO_4)_2$ + 0.0042 $LiCoPO_4$ + 0.0675 $\underline{Co_9S_8}$ + 0.2489 Li_2SO_4
G	0.9289	0.1067 $Co_3(PO_4)_2$ + 0.0089 CoO + 0.0667 $\underline{Co_9S_8}$ + 0.2489 Li_2SO_4
H	0.9778	0.0333 $Co_3(PO_4)_2$ + 0.7111 CoO + 0.1667 $CoSO_4$ + 0.0778 Li_2SO_4
I	0.9836	0.0246 $Co_3(PO_4)_2$ + 0.2623 $\underline{Co_3O_4}$ + 0.1230 $CoSO_4$ + 0.0574 Li_2SO_4
J	0.9844	0.0469 $CoPO_4$ + 0.2734 $\underline{Co_3O_4}$ + 0.1172 $CoSO_4$ + 0.0547 Li_2SO_4
(b) $LiCoO_2$		
A	0.5000	0.5000 $\underline{CoS_2}$ + 0.2500 $Li_4P_2S_6$ + 0.7500 Li_3PS_4 + 0.2500 Li_3PO_4
B	0.6667	0.1667 $\underline{CoS_2}$ + 0.6667 Li_3PS_4 + 0.1667 $\underline{Co_3S_4}$ + 0.3333 Li_3PO_4
C	0.8571	0.2143 $\underline{CoS_2}$ + 0.2857 Li_2S + 0.2143 $\underline{Co_3S_4}$ + 0.4286 Li_3PO_4
D	0.8675	0.2651 Li_2S + 0.2892 $\underline{Co_3S_4}$ + 0.0361 Li_2SO_4 + 0.3976 Li_3PO_4
E	0.8963	0.2075 Li_2S + 0.0996 $\underline{Co_9S_8}$ + 0.1369 Li_2SO_4 + 0.3112 Li_3PO_4
F	0.9135	0.1015 $\underline{Co_9S_8}$ + 0.2307 Li_2O + 0.1396 Li_2SO_4 + 0.2595 Li_3PO_4
G	0.9196	0.0804 Li_6CoO_4 + 0.0932 $\underline{Co_9S_8}$ + 0.1383 Li_2SO_4 + 0.2412 Li_3PO_4
H	0.9677	0.0323 Li_6CoO_4 + 0.3548 Li_2SO_4 + 0.0968 Li_3PO_4 + 0.9355 $\underline{Co}$
I	0.9888	0.1199 Li_6CoO_4 + 0.8689 CoO + 0.1236 Li_2SO_4 + 0.0337 Li_3PO_4
(c) Li		
A	0.5000	1.0000 Li_3PS_4 + 0.2500 $Li_4P_2S_6$
B	0.7500	0.3750 $Li_4P_2S_6$ + 0.5000 Li_2S
C	0.9375	0.6875 Li_2S + 0.1875 P
D	0.9391	0.0261 LiP_7 + 0.6696 Li_2S
E	0.9421	0.0248 Li_3P_7 + 0.6364 Li_2S
F	0.9474	0.1579 LiP + 0.5789 Li_2S
G	0.9600	0.1200 Li_3P + 0.4400 Li_2S

[a]Poor electronic insulators are indicated with an underline.

insulators (*e.g.*, Co and Co_3O_4 and Co_9S_8)[42,43] in either the charged or discharged state.

Unlike $LiCoO_2$, the interfaces between SCEs and other common electrode materials such as the olivine $LiFePO_4$ and spinel $LiMn_2O_4$ are much less studied. Using the same methodology, we investigated the phase equilibria between $Li_7P_3S_{11}$ and the charged olivine $FePO_4$ (Figure S3 in the SI) and charged spinel Mn_2O_4 (Figure S5 in the SI) cathodes. Although poor electronic insulators such as FeS_2 and MnS_2 appear at certain cathode/SCE ratios x, the phases formed close to the cathode, *i.e.*, with largest values of x, are all fully electronically insulating phases, which may form good passivation layers against further reactions.

Electronic Structure. The electronic band gap, which can be obtained from electronic structure calculations, is often considered as the upper bound of the intrinsic electrochemical window for the SCE studied. The electronic band structure of $Li_7P_3S_{11}$ is illustrated in Figure 6a. A minimum band gap of 3.9 eV is found to be indirect from X to N, which suggests that $Li_7P_3S_{11}$ is a wide band gap insulator. Our calculated band gap also agrees with the value of 3.5 eV previously calculated by Xiong et al.[44] Figure 6b displays the stacked projected density of states of the compound. The valence band maximum is mainly contributed to by the p states in S, whereas the p states in both P and S mostly contribute to the conduction band minimum. We have also compared the electronic structure of $Li_7P_3S_{11}$ calculated using the PBE functional to that calculated with the HSE functional. In general, the electronic structure is similar between the two functionals, except that the PBE band gap is significantly smaller at 2.6 eV, which agrees with the value of 2.1 eV by Xiong et al.[44]

Surface Energies and Wulff Shape. Figure 7 shows the calculated Wulff shape and surface energies of the six low-index orientations for $Li_7P_3S_{11}$. The (100), (10$\bar{1}$), and (010) surfaces are the most stable with surface energies of 0.1, 0.12, and 0.16 J/m^2, respectively. Using the obtained surface energies, the Wulff construction of $Li_7P_3S_{11}$ was carried out for the equilibrium morphology of $Li_7P_3S_{11}$ crystal, as shown in Figure 7. The relative area contributions $p(\mathbf{n}) = A_\mathbf{n}/A_{tot}$ for the six orientations $\mathbf{n}$ were also estimated. Here, $A_{tot} = \sum_\mathbf{n} A_\mathbf{n}$ is the total surface area over the six orientations $\mathbf{n}$.

Three orientations, (100), (10$\bar{1}$), and (010) contribute more than 90% of the total surface area of the Wulff shape. The calculated Wulff shape is in good qualitative agreement with our cold-pressed sample (Figure 2a), which shows large relatively isotropic crystals with few facets.

Li^+ Conductivity. The theoretically calculated and experimentally measured Arrhenius plot for $Li_7P_3S_{11}$ is shown together in Figure 8a. For the experimentally measured Arrhenius plot, electrochemical impedance measurements were conducted where the Arrhenius behavior was calculated by using the real-axis impedance intercept in the Nyquist plot as the total impedance (see Figure S7 and S8 in the SI). The activation energy (E_a) extracted from the theoretically

DOI: 10.1021/acsami.6b00833
ACS Appl. Mater. Interfaces XXXX, XXX, XXX−XXX

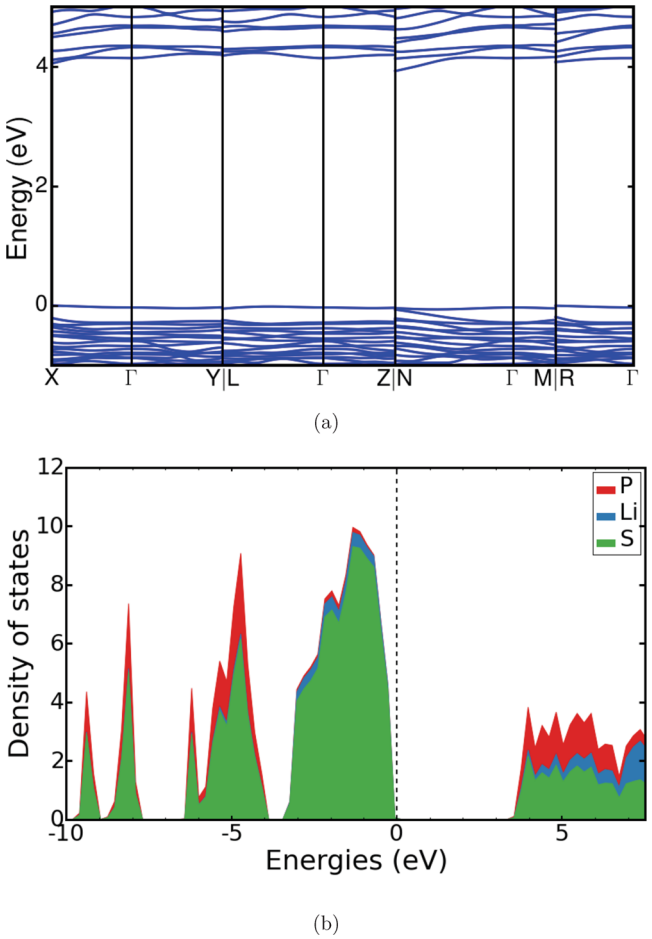

Figure 6. (a) Electronic band structure and (b) electronic stacked projected density of states of $Li_7P_3S_{11}$ using HSE hybrid functionals.

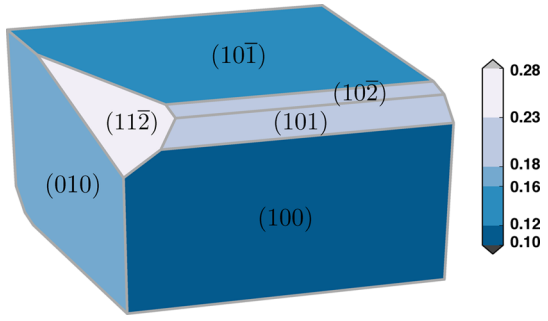

Figure 7. Wulff shape of $Li_7P_3S_{11}$ constructed using the six low-index surfaces. The values given at the color bar are the energy scale of the surface in J/m^2. The relative area contributions of the (100), (10$\bar{1}$), and (010) surfaces are 38%, 29%, and 25%, respectively.

calculated fitting is 187 meV, in excellent agreement with experimental value of 180 meV for the SPS sample (209 meV for the cold-pressed sample). The theoretical room-temperature diffusivity ($D(T$=300K)) is obtained by linear extrapolation and is found to be 5.7 × 10^{-7}cm^2/s. This is in line with the previous Li-ion diffusion measurements using the pulsed-gradient spin−echo (PGSE) nuclear magnetic resonance (NMR) technique, where the Li-ion diffusivity is 10^{-8}−10^{-7} cm^2/s at temperatures of 303−353 K.[45] It is worth pointing out that, in the AIMD calculations at 700 K or below, the one-dimensional MSD along the *b*-axis is nearly a factor of 2 higher

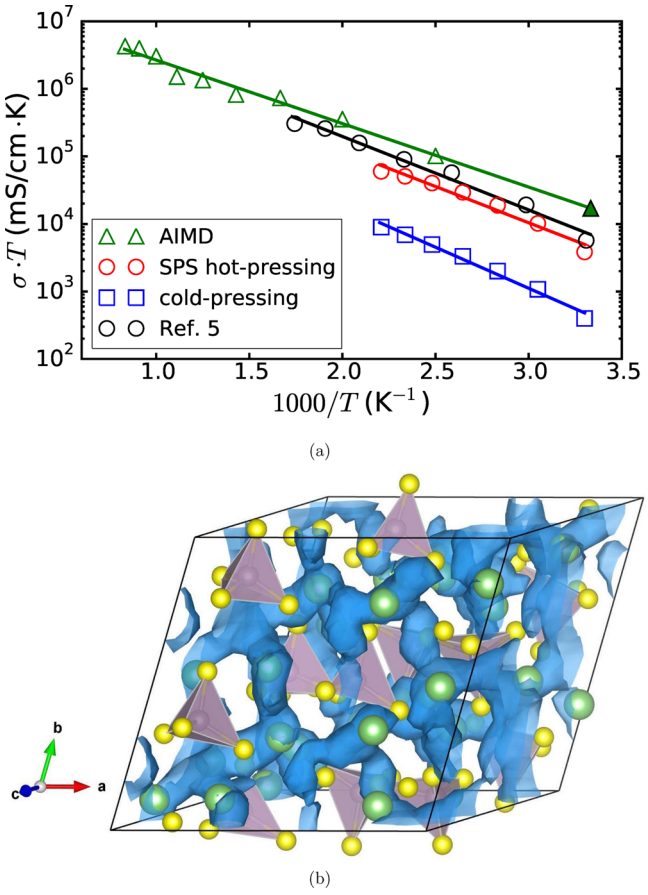

Figure 8. (a) Arrhenius plots of $Li_7P_3S_{11}$ obtained from AIMD simulations (green triangles) and conductivity measurements of cold-pressed sample (blue squares) and SPS hot-pressed sample (red circles). The Arrhenius plot by Seino et al.[5] that shows the highest room-temperature ionic conductivity of 17 mS/cm to date is also shown (black circles) for comparison. The filled triangle corresponds to the linearly extrapolated room-temperature conductivity from AIMD. (b) Isosurface of the probability density distribution (dark blue) $P(\mathbf{r})$ of Li^+ ions in $Li_7P_3S_{11}$ superionic conductor at 600 K, with P = 0.001.

than along the other two axes, which is consistent with the nudged elastic band results of Lepley and Holzwarth.[19] The corresponding room-temperature ionic conductivity (σ-(T=300K)) is evaluated as 57 mS cm^{-1}, and the estimated error bar is between 50 and 65 mS cm^{-1}. For the experimentally obtained values, there is a significant increase of $\sigma(T$=300K) from the cold-press-sintered (1.3 mS cm^{-1}) to the SPS pellet (11.6 mS cm^{-1}). This increase in conductivity is similar to the densified $Li_7P_3S_{11}$ pellets obtained via hot-press sintering (17 mS cm^{-1}).[5] However, the measured ionic conductivity is significantly lower than the one derived from the AIMD simulations. We will discuss the reasons for this discrepancy in Discussion. We note that the lattice parameters predicted by the PBE functional are about 3% higher than the experimental values. To exclude functional limitations as a potential source of error, we also performed a full relaxation and AIMD simulation using the PBEsol functional, which is known to provide much more accurate predictions of lattice parameters.[46] The PBEsol lattice parameters differ from the experimental values by only 1%, but the extrapolated room-temperature conductivity is 60.5 mS cm^{-1}, which is very close to the PBE value.

DOI: 10.1021/acsami.6b00833
ACS Appl. Mater. Interfaces XXXX, XXX, XXX−XXX

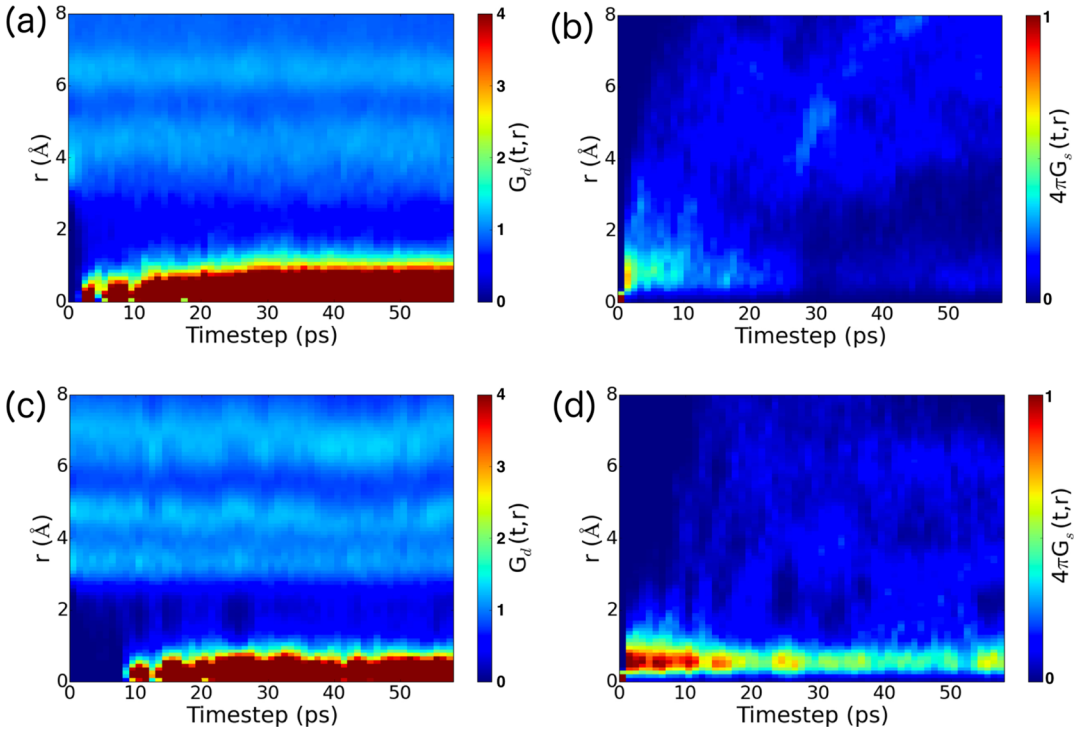

Figure 9. Distinct part of the van Hove correlation function (G_d) for lithium in (a) $Li_7P_3S_{11}$ and (c) $Li_{10}GeP_2S_{12}$. The self-part of the van Hove correlation function (G_s) for lithium in (b) $Li_7P_3S_{11}$ and (d) $Li_{10}GeP_2S_{12}$. Both G_d and G_s are functions of the average Li−Li pair distance r and time step after thermal equilibration at 600 K.

Correlated Li^+ Motions and Framework Motions. Figure 8b shows the probability density distribution ($P(\mathbf{r})$) of Li^+ at 600 K. It is clear that the diffusion pathway forms a 3D network in which all of the Li^+ sites are connected to one another via empty S_4 tetrahedra. Given that the Li sites are fully occupied in this compound, this suggests that the Li ionic motion is highly collective, in agreement with previous experimental[45] and computational investigations.[47,48] This is also in contrast to other Li superionic conductors where defects (*e.g.*, Li^+ vacancy) are required to facilitate the Li-ion diffusion.[38]

The van Hove correlation function (G), which can be divided into the self part (G_s) and the distinct part (G_d), is often adopted for investigating the highly correlated ionic motions. Figure 9a plots G_d for lithium after thermal equilibration in which a large magnitude of G_d is reached for r < 1 Å soon after t = 2 ps at 600 K. We relate this to the correlation time scale of the lithium-ion motions. This is also a strong indication of collective motions because for a given reference lithium ion at site r, it shows that other lithium ions move and occupy that site at later time moments when this reference ion diffuses away. Moreover, G_d is peaked but with smaller magnitude and more broadened for r between 3.5 and 4.5 Å, and also between 6 and 7 Å. The former is close to the shortest lithium−lithium distance in the initially relaxed atomic structure (see Figure S9). The presence of these peaks also implies that on average each lithium ion is surrounded by some of the other lithium ions during the entire diffusion process. Figure 9b shows the G_s for lithium as functions of r and t after thermal equilibration process at 600 K. It shows that G_s remains large for r < 1 Å before t < 10 ps, and then its value decreases. This suggests that the lithium ions tend to diffuse away from their initial positions to neighboring lithium sites.

For comparison, the G_d and G_s plots for another superionic conductor $Li_{10}GeP_2S_{12}$ are presented in Figure 9c,d, respectively. As indicated in Figure 9c, we observe that the time scale of correlation in $Li_{10}GeP_2S_{12}$ is around 10 ps at 600 K, which is longer than that of $Li_7P_3S_{11}$. Similar to $Li_7P_3S_{11}$, there are two broadened peaks for r (i) between 3 and 5 Å and (ii) between 6 and 7 Å (see also Figure S10). The former region relates to the shortest lithium−lithium distance in the initially relaxed structure. Comparing the G_s, we may also note that Li^+ in $Li_{10}GeP_2S_{12}$ has a much higher probability of returning to their initial positions and staying there for a longer time duration than in $Li_7P_3S_{11}$. These findings are consistent with the lower ionic conductivity of $Li_{10}GeP_2S_{12}$ compared to that of $Li_7P_3S_{11}$.

We also investigated the motion of the framework ions in the AIMD trajectories. We find no evidence of framework melting at all temperatures. The P−S bond distances show very small fluctuations of <0.1 Å during the simulations, whereas S−S distances within the same tetrahedron show a slightly larger fluctuation of ∼0.2 Å. S−S distance fluctuations become much larger for S in different tetrahedra. We also find that the P-bridging S−P bond angle in the P_2S_7 ditetrahedra fluctuates by around 5° in the simulations.

DISCUSSION

In this work, we performed a comprehensive DFT and experimental investigation of the $Li_7P_3S_{11}$ glass-ceramic solid electrolyte. A good solid electrolyte must satisfy several criteria, namely, phase stability, a wide electrochemical stability, and a high Li^+ conductivity.

In terms of stability, we find that though $Li_7P_3S_{11}$ is a metastable phase at 0 K, it becomes stable at above 630 K (∼360 °C) when vibrational entropic contributions are taken into account. Our estimated transition temperature of 630 K

DOI: 10.1021/acsami.6b00833
ACS Appl. Mater. Interfaces XXXX, XXX, XXX−XXX

(~360 °C) agrees well with the experimental crystallization temperature of 553 K (280 °C). However, the predicted phase equilibria of $Li_7P_3S_{11}$ depends significantly on the sulfur chemical potential. When a corrected sulfur energy (to reproduce experimental formation energies of sulfides) is used, the predicted phase equilibrium comprises γ-Li_3PS_4 and P_2S_5. When an uncorrected sulfur energy is used, the phase equilibrium contains $Li_4P_2S_6$ and S. The latter phase equilibrium is actually more consistent with previous experimental results, which found $Li_4P_2S_6$ as one of the primary decomposition products under certain synthesis conditions at >633 K (360 °C).[12] There are two reasons for this apparent discrepancy. First, $Li_4P_2S_6$ is a disordered structure, and thus may be entropically more stable at higher temperatures. Second, any sulfur loss at high temperatures would also result in the latter phase equilibrium becoming significantly more favorable, in line with Le Châtelier's principle. We believe that, at lower temperatures, the phase equilibria should indeed comprise the low-temperature γ-Li_3PS_4 and P_2S_5 phases. Furthermore, both $Li_4P_2S_6$ and Li_3PS_4 are observed during solid-state synthesis of $Li_2S-P_2S_5$ glass-ceramics.[12]

In agreement with previous DFT results of Zhu et al.,[49] we find that $Li_7P_3S_{11}$ is unlikely to be intrinsically stable against either the cathode or anode. At the Li metal anode, the predicted products formed are generally reasonable ionic conductors and poor electronic conductors that should form a good passivation layer. Somewhat surprisingly, it is the $Li_7P_3S_{11}$/cathode interface that might pose stability issues, depending on the cathode chemistry selected. For the olivine $LiFePO_4$ and spinel $LiMn_2O_4$, we find that the predicted phase equilibria for the $Li_7P_3S_{11}$/charged cathode interface contains fully electronic insulating, but ionic conducting, phases near the cathode. These phases are potential candidates for a good passivation layer, which can stabilize the cathode/$Li_7P_3S_{11}$ interface during battery operations. For the layered $LiCoO_2$ cathode on the other hand, we find that poor electronic insulators are present at all stoichiometries, in agreement with previous experimental studies.[41] This suggests that the $Li_7P_3S_{11}/LiCoO_2$ interface is unstable against further propagation of the reaction front, and buffer layers such as $LiNbO_3$ need to be introduced to improve stability and improve rate capability.[41,50,51] To the authors' knowledge, there have been no extensive study done on the interactions between different cathode and SCE chemistries. The DFT results show that the selection of the cathode chemistry is likely to be of critical importance in designing an all-solid-state battery.

The results of the AIMD simulations are somewhat surprising. Though there is excellent agreement between the computed and experimentally measured diffusion activation energy E_a, the extrapolated conductivity at 300 K of 57 mS cm^{-1} is a factor of 3−5 higher than the experimental values, which are between 11.6 and 17 mS cm^{-1}.[5] One possible explanation for this discrepancy is that there is a phase transition that occurs between 300 K and the temperatures of the AIMD simulations. However, the minimum temperature in our AIMD simulations is 400 K, one of the lowest temperatures ever performed for a solid-state conductor, and it is unlikely there is a phase transition between 300 and 400 K that would significantly alter the Li diffusion behavior. Our hypothesis therefore is that the intrinsic bulk Li^+ conductivity of the $Li_7P_3S_{11}$ crystal is indeed significantly higher than the currently achieved conductivities thus far, and grain boundary limitations are responsible for the lower experimental conductivities. In fact, until recently, the ionic conductivity of $Li_7P_3S_{11}$ obtained in the experiments was only as high as 5.2 mS cm^{-1}.[13] It is through the reduction of grain boundary impedance by densification via hot-press sintering or SPS that the highest room-temperature conductivities have been achieved thus far for this material.[5] Another recent experiment also showed that further optimization of the glass-ceramic by reducing the amorphous glass phase detected via p-MAS could improve the overall conductivity of the material.[52]

We further support this hypothesis with the observation that despite having fairly similar E_a, the measured conductivities of the cold-pressed and SPS samples differ by more than 1 order of magnitude. The highly granular morphology of the cold-pressed sample is expected to have significantly higher grain boundary resistance than that of the SPS made pellets. Given that the experimental and computed E_a are all similar, we believe that the local structure and fundamental diffusion mechanisms are similar in both the amorphous grain boundary and the bulk phase. We speculate that the vastly different conductivities are therefore due to either a concentration effect from possible Li depletion at the grain boundaries or a difference in the hopping attempt frequency prefactor in the Arrhenius relation. The testing of these hypotheses will be the subject of future work.

We attempted to obtain further insights into the topological reasons for the high Li^+ conductivity of $Li_7P_3S_{11}$. Consistent with previous analyses,[17,18] the Li probability density distribution shows that Li^+ diffusion occurs through interconnected S_4 tetrahedra sites. This tetrahedron-to-tetrahedron hopping in a bcc-like anion framework has been identified by Wang et al.[53] as a low-barrier mechanism. The van Hove correlation function analysis also highlights the highly correlated nature of the Li motion in $Li_7P_3S_{11}$, where the site vacated by a diffusing Li^+ is rapidly occupied by another Li^+, resulting in a significantly lower probability of a "back-hop" compared to $Li_{10}GeP_2S_{12}$. Also, the G_d of $Li_7P_3S_{11}$ is peaked at r between 3.5 and 4.5 Å during the time period studied, which corresponds to the average Li−Li separation during diffusion. This is in good agreement with a recent experimental measurement in which the jump length of Li ions during Li^+ migration is estimated at 4.3 Å.[48] Finally, we also find that although the framework PS_4 tends to remain relatively rigid throughout the simulations, significant flexing of the P_2S_7 ditetrahedra is observed. This is consistent with the recent experimental finding that the motional fluctuations of the framework polyhedrons contribute to the fast Li-ion diffusion.[54]

CONCLUSIONS

To conclude, we have performed a comprehensive computational and experimental investigation of the performance limits of the $Li_7P_3S_{11}$ superionic conductor. Our work has shed important insights into the phase and electrochemical stability and Li^+ conductivity in this material. We find that the stability of the $Li_7P_3S_{11}$/cathode interface depends critically on the cathode chemistry. Unlike layered $LiCoO_2$ cathode, DFT calculations predict that the olivine $LiFePO_4$ and spinel $LiMn_2O_4$ cathodes are likely to form more stable passivating phases with $Li_7P_3S_{11}$. Furthermore, while significant increase from cold-press-sintered to SPS pellet was observed due to densification, the predicted bulk Li^+ conductivity of $Li_7P_3S_{11}$ is 57 mS cm^{-1}, significantly higher than the values achieved experimentally thus far. The significant difference in Li^+ of $Li_7P_3S_{11}$ synthesis via cold-pressed sintering and SPS shows that

DOI: 10.1021/acsami.6b00833
ACS Appl. Mater. Interfaces XXXX, XXX, XXX−XXX

grain boundary conductivity is likely limiting the overall Li^+ conductivity in $Li_7P_3S_{11}$. Further optimization of overall Li^+ conductivities in $Li_7P_3S_{11}$ should therefore be possible.

■ ASSOCIATED CONTENT

Supporting Information

The Supporting Information is available free of charge on the ACS Publications website at DOI: 10.1021/acsami.6b00833.

Computational details of phonons and thermodynamic properties of $Li_7P_3S_{11}$, introduction of van Hove correlation functions, lithium grand potential phase diagrams, pseudobinary phase diagrams of $Li_7P_3S_{11}$ with olivine $LiFePO_4$ and spinel $LiMn_2O_4$, static pair distribution functions of $Li_7P_3S_{11}$ and $Li_{10}GeP_2S_{12}$, and $Li_7P_3S_{11}$ glass-ceramic Nyquist curves from cold-pressed and SPS hot-pressed samples (PDF)

■ AUTHOR INFORMATION

Corresponding Authors

*(Y.S.M.) E-mail: shmeng@ucsd.edu.

*(S.P.O.) E-mail: ongsp@ucsd.edu.

Notes

The authors declare no competing financial interest.

■ ACKNOWLEDGMENTS

This work was primarily supported by the U.S. Department of Energy, Office of Science, Basic Energy Sciences under Award Nos. DE-SC0012118 (computational studies) and DE-SC0002357 (experimental work) . We also acknowledge computational resources provided by Triton Shared Computing Cluster (TSCC) at the University of California, San Diego, the National Energy Research Scientific Computing Center (NERSC), and the Extreme Science and Engineering Discovery Environment (XSEDE) supported by National Science Foundation under Grant No. ACI-1053575.

■ REFERENCES

(1) Inaguma, Y.; Liquan, C.; Itoh, M.; Nakamura, T.; Uchida, T.; Ikuta, H.; Wakihara, M. High Ionic Conductivity in Lithium Lanthanum Titanate. *Solid State Commun.* **1993**, *86*, 689−693.

(2) Murugan, R.; Thangadurai, V.; Weppner, W. Fast Lithium Ion Conduction in Garnet-type $Li_7La_3Zr_2O_{12}$. *Angew. Chem., Int. Ed.* **2007**, *46*, 7778−7781.

(3) Kamaya, N.; Homma, K.; Yamakawa, Y.; Hirayama, M.; Kanno, R.; Yonemura, M.; Kamiyama, T.; Kato, Y.; Hama, S.; Kawamoto, K.; Mitsui, A. A Lithium Superionic Conductor. *Nat. Mater.* **2011**, *10*, 682−686.

(4) Yamane, H.; Shibata, M.; Shimane, Y.; Junke, T.; Seino, Y.; Adams, S.; Minami, K.; Hayashi, A.; Tatsumisago, M. Crystal Structure of a Superionic Conductor, $Li_7P_3S_{11}$. *Solid State Ionics* **2007**, *178*, 1163−1167.

(5) Seino, Y.; Ota, T.; Takada, K.; Hayashi, A.; Tatsumisago, M. A Sulphide Lithium Super Ion Conductor Is Superior to Liquid Ion Conductors for Use in Rechargeable Batteries. *Energy Environ. Sci.* **2014**, *7*, 627−631.

(6) Tarascon, J.; Armand, M. Issues and Challenges Facing Rechargeable Lithium Batteries. *Nature* **2001**, *414*, 359−367.

(7) Armand, M.; Tarascon, J. Building Better Batteries. *Nature* **2008**, *451*, 652−657.

(8) Xu, K. Electrolytes and Interphases in Li-ion Batteries and Beyond. *Chem. Rev.* **2014**, *114*, 11503−11618.

(9) Mo, Y.; Ong, S. P.; Ceder, G. First Principles Study of the $Li_{10}GeP_2S_{12}$ Lithium Super Ionic Conductor Material. *Chem. Mater.* **2012**, *24*, 15−17.

(10) Mizuno, F.; Hayashi, a.; Tadanaga, K.; Tatsumisago, M. New, Highly Ion-conductive Crystals Precipitated from Li_2S-P_2S_5 Glasses. *Adv. Mater.* **2005**, *17*, 918−921.

(11) Mizuno, F.; Hayashi, a.; Tadanaga, K.; Tatsumisago, M. High Lithium Ion Conducting Glass-Ceramics in the System Li_2S-P_2S_5. *Solid State Ionics* **2006**, *177*, 2721−2725.

(12) Minami, K.; Hayashi, A.; Tatsumisago, M. Preparation and Characterization of Superionic Conducting $Li_7P_3S_{11}$ Crystal from Glassy Liquids. *J. Ceram. Soc. Jpn.* **2010**, *118*, 305−308.

(13) Minami, K.; Hayashi, A.; Tatsumisago, M. Crystallization Process for Superionic $Li_7P_3S_{11}$ Glass-ceramic Electrolytes. *J. Am. Ceram. Soc.* **2011**, *94*, 1779−1783.

(14) Ong, S. P.; Mo, Y.; Richards, W. D.; Miara, L.; Lee, H. S.; Ceder, G. Phase Stability, Electrochemical Stability and Ionic Conductivity of the $Li_{10\pm1}MP_2X_{12}$ (M = Ge, Si, Sn, Al or P, and X = O, S or Se) Family of Superionic Conductors. *Energy Environ. Sci.* **2013**, *6*, 148−156.

(15) Bron, P.; Johansson, S.; Zick, K.; Schmedt auf der Gunne, J.; Dehnen, S. S.; Roling, B. $Li_{10}SnP_2S_{12}$ - An Affordable Lithium Superionic Conductor $Li_{10}SnP_2S_{12}$ - An Affordable Lithium Superionic Conductor. *J. Am. Chem. Soc.* **2013**, *135*, 15694−15697.

(16) Kuhn, A.; Duppel, V.; Lotsch, B. V. Tetragonal $Li_{10}GeP_2S_{12}$ and Li_7GePS_8 - Exploring the Li Ion Dynamics in LGPS Li Electrolytes. *Energy Environ. Sci.* **2013**, *6*, 3548−3552.

(17) Onodera, Y.; Mori, K.; Otomo, T.; Sugiyama, M.; Fukunaga, T. Structural Evidence for High Ionic Conductivity of $Li_7P_3S_{11}$ Metastable Crystal. *J. Phys. Soc. Jpn.* **2012**, *81*, 044802.

(18) Onodera, Y.; Mori, K.; Otomo, T.; Arai, H.; Uchimoto, Y.; Ogumi, Z.; Fukunaga, T. Structural Origin of Ionic Conductivity for $Li_7P_3S_{11}$ Metastable Crystal by Neutron And X-ray Diffraction. *J. Phys.: Conf. Ser.* **2014**, *502*, 012021.

(19) Lepley, N. D.; Holzwarth, N. a. W. Computer Modeling of Crystalline Electrolytes: Lithium Thiophosphates and Phosphates. *J. Electrochem. Soc.* **2012**, *159*, A538−A547.

(20) Kresse, G.; Furthmüller, J. Efficient Iterative Schemes for Ab Initio Total-energy Calculations Using a Plane-wave Basis Set. *Phys. Rev. B: Condens. Matter Mater. Phys.* **1996**, *54*, 11169−11186.

(21) Blöchl, P. E. Projector Augmented-wave Method. *Phys. Rev. B: Condens. Matter Mater. Phys.* **1994**, *50*, 17953−17979.

(22) Perdew, J.; Burke, K.; Ernzerhof, M. Generalized Gradient Approximation Made Simple. *Phys. Rev. Lett.* **1996**, *77*, 3865−3868.

(23) Monkhorst, H.; Pack, J. Special Points for Brillouin-zone Integrations. *Phys. Rev. B* **1976**, *13*, 5188−5192.

(24) Ong, S. P.; Richards, W. D.; Jain, A.; Hautier, G.; Kocher, M.; Cholia, S.; Gunter, D.; Chevrier, V. L.; Persson, K. a.; Ceder, G. Python Materials Genomics (Pymatgen): A Robust, Open-Source Python Library for Materials Analysis. *Comput. Mater. Sci.* **2013**, *68*, 314−319.

(25) Ong, S. P.; Wang, L.; Kang, B.; Ceder, G. Li-Fe-P-O_2 Phase Diagram from First Principles Calculations. *Chem. Mater.* **2008**, *20*, 1798−1807.

(26) Jain, A.; Ong, S. P.; Hautier, G.; Chen, W.; Richards, W. D.; Dacek, S.; Cholia, S.; Gunter, D.; Skinner, D.; Ceder, G.; Persson, K. a. Commentary: The Materials Project: A Materials Genome Approach to Accelerating Materials Innovation. *APL Mater.* **2013**, *1*, 011002.

(27) Ong, S. P.; Cholia, S.; Jain, A.; Brafman, M.; Gunter, D.; Ceder, G.; Persson, K. a. The Materials Application Programming Interface (API): A Simple, Flexible and Efficient API for Materials Data Based on REpresentational State Transfer (REST) Principles. *Comput. Mater. Sci.* **2015**, *97*, 209−215.

(28) Wang, L.; Maxisch, T.; Ceder, G. Oxidation Energies of Transition Metal Oxides within the GGA + U Framework. *Phys. Rev. B: Condens. Matter Mater. Phys.* **2006**, *73*, 195107.

(29) Zhu, Z.; Chu, I.-H.; Deng, Z.; Ong, S. P. Role of Na^+ Interstitials and Dopants in Enhancing the Na^+ Conductivity of the Cubic Na_3PS_4 Superionic Conductor. *Chem. Mater.* **2015**, *27*, 8318−8325.

(30) Togo, A.; Oba, F.; Tanaka, I. First-Principles Calculations of the Ferroelastic Transition between Rutile-type and $CaCl_2$-type SiO_2 at High Pressures. *Phys. Rev. B: Condens. Matter Mater. Phys.* **2008**, *78*, 134106.

DOI: 10.1021/acsami.6b00833
ACS Appl. Mater. Interfaces XXXX, XXX, XXX−XXX

(31) Baroni, S.; de Gironcoli, S. D.; Dal Corso, A.; Giannozzi, P. Phonons and Related Crystal Properties from Density-Functional Perturbation Theory. *Rev. Mod. Phys.* **2001**, *73*, 515−562.
(32) Miara, L. J.; Richards, W. D.; Wang, Y. E.; Ceder, G. First-principles Studies on Cation Dopants and Electrolyte-cathode Interphases for Lithium Garnets. *Chem. Mater.* **2015**, *27*, 4040−4047.
(33) Ong, S. P.; Ceder, G. Investigation of the Effect of Functional Group Substitutions on the Gas-phase Electron Affinities and Ionization Energies of Room-temperature Ionic Liquids Ions Using Density Functional Theory. *Electrochim. Acta* **2010**, *55*, 3804−3811.
(34) Heyd, J.; Scuseria, G. E.; Ernzerhof, M. Hybrid Functionals Based on a Screened Coulomb Potential. *J. Chem. Phys.* **2003**, *118*, 8207−8215.
(35) Heyd, J.; Scuseria, G. E.; Ernzerhof, M. Erratum: "Hybrid Functionals Based on a Screened Coulomb Potential" [J. Chem. Phys. 118, 8207 (2003)]. *J. Chem. Phys.* **2006**, *124*, 219906.
(36) Heyd, J.; Scuseria, G. E. Efficient Hybrid Density Functional Calculations in Solids: Assessment of the Heyd-Scuseria-Ernzerhof Screened Coulomb Hybrid Functional. *J. Chem. Phys.* **2004**, *121*, 1187−1192.
(37) Wang, L.; Zhou, F.; Meng, Y. S.; Ceder, G. First-Principles Study of Surface Properties of $LiFePO_4$: Surface Energy, Structure, Wulff Shape, and Surface Redox Potential. *Phys. Rev. B: Condens. Matter Mater. Phys.* **2007**, *76*, 165435.
(38) Deng, Z.; Radhakrishnan, B.; Ong, S. P. Rational Composition Optimization of the Lithium-rich $Li_3OCl_{1-x}Br_x$ Anti-perovskite Superionic Conductors. *Chem. Mater.* **2015**, *27*, 3749−3755.
(39) *pymatgen-diffusion*. http://dx.doi.org/10.5281/zenodo.46807 (accessed Mar. 2, 2016).
(40) Sakuda, A.; Hayashi, A.; Tatsumisago, M. Interfacial Observation Between $LiCoO_2$ Electrode and Li_2S-P_2S_5 Solid Electrolytes of All-solid-state Lithium Secondary Batteries Using Transmission Electron Microscopy. *Chem. Mater.* **2010**, *22*, 949−956.
(41) Mizuno, F.; Iba, H. Research on Electrode-Electrolyte Interfaces of Innovative New Generation Batteries. *Honolulu PRIME 2012*, Meeting Abstract 1196; The Electrochemical Society: Pennington, NJ, USA, 2012.
(42) Ramos, M.; Berhault, G.; Ferrer, D. a.; Torres, B.; Chianelli, R. R. HRTEM and Molecular Modeling of the MoS_2-Co_9S_8 Interface: Understanding the Promotion Effect in Bulk HDS Catalysts. *Catal. Sci. Technol.* **2012**, *2*, 164.
(43) Qiao, L.; Xiao, H. Y.; Meyer, H. M.; Sun, J. N.; Rouleau, C. M.; Puretzky, a. a.; Geohegan, D. B.; Ivanov, I. N.; Yoon, M.; Weber, W. J.; Biegalski, M. D. Nature of the Band Gap and Origin of the Electro-/Photo-activity of Co_3O_4. *J. Mater. Chem. C* **2013**, *1*, 4628−4633.
(44) Xiong, K.; Longo, R.; Kc, S.; Wang, W.; Cho, K. Behavior of Li Defects in Solid Electrolyte Lithium Thiophosphate $Li_7P_3S_{11}$: A First Principles Study. *Comput. Mater. Sci.* **2014**, *90*, 44−49.
(45) Hayamizu, K.; Aihara, Y. Lithium Ion Diffusion in Solid Electrolyte $(Li_2S)_7(P_2S_5)_3$ Measured by Pulsed-gradient Spin-echo 7Li NMR Spectroscopy. *Solid State Ionics* **2013**, *238*, 7−14.
(46) Perdew, J.; Ruzsinszky, A.; Csonka, G.; Vydrov, O.; Scuseria, G.; Constantin, L.; Zhou, X.; Burke, K. Restoring the Density-gradient Expansion for Exchange in Solids and Surfaces. *Phys. Rev. Lett.* **2008**, *100*, 136406.
(47) Yamasaki, H.; Shirasawa, A.; Nishino, N. DFT and MD Simulations of Li-Ion Pathway in Solid State Sulfide $Li_7P_3S_{11}$ Electrolyte. *218th ECS Meeting*, Meeting Abstract 600; The Electrochemical Society: Pennington, NJ, USA, 2010.
(48) Mori, K.; Enjuji, K.; Murata, S.; Shibata, K.; Kawakita, Y.; Yonemura, M.; Onodera, Y.; Fukunaga, T. Direct Observation of Fast Lithium-Ion Diffusion in a Superionic Conductor: $Li_7P_3S_{11}$ Metastable Crystal. *Phys. Rev. Appl.* **2015**, *4*, 054008.
(49) Zhu, Y.; He, X.; Mo, Y. Origin of Outstanding Stability in the Lithium Solid Electrolyte Materials: Insights from Thermodynamic Analyses Based on First Principles Calculations. *ACS Appl. Mater. Interfaces* **2015**, *7*, 23685−23693.
(50) Takada, K.; Ohta, N.; Zhang, L.; Fukuda, K.; Sakaguchi, I.; Ma, R.; Osada, M.; Sasaki, T. Interfacial Modification for High-power Solid-state Lithium Batteries. *Solid State Ionics* **2008**, *179*, 1333−1337.
(51) Takada, K.; Ohta, N.; Zhang, L.; Xu, X.; Hang, B. T.; Ohnishi, T.; Osada, M.; Sasaki, T. Interfacial Phenomena in Solid-state Lithium Battery with Sulfide Solid Electrolyte. *Solid State Ionics* **2012**, *225*, 594−597.
(52) Seino, Y.; Nakagawa, M.; Senga, M.; Higuchi, H.; Takada, K.; Sasaki, T. Analysis of the Structure and Degree of Crystallisation of $70Li_2S$-$30P_2S_5$ Glass Ceramic. *J. Mater. Chem. A* **2015**, *3*, 2756−2761.
(53) Wang, Y.; Richards, W. D.; Ong, S. P.; Miara, L. J.; Kim, J. C.; Mo, Y.; Ceder, G. Design Principles for Solid-state Lithium Superionic Conductors. *Nat. Mater.* **2015**, *14*, 1026−1031.
(54) Murakami, M.; Shimoda, K.; Shiotani, S.; Mitsui, A.; Ohara, K.; Onodera, Y.; Arai, H.; Uchimoto, Y.; Ogumi, Z. Dynamical Origin of Ionic Conductivity for $Li_7P_3S_{11}$ Metastable Crystal as Studied by $^{6/7}$Li and ^{31}P Solid-State NMR. *J. Phys. Chem. C* **2015**, *119*, 24248−24254.

DOI: 10.1021/acsami.6b00833
ACS Appl. Mater. Interfaces XXXX, XXX, XXX−XXX